arXiv:2603.09102v1 [physics.atom-ph] 10 Mar 2026

Strong Electron Correlation Identified in Planetary Atomic Structure

Xinglong Yu[1,2,7†], Yongyan Han[3†], Zhenjie Shen[2*], Yong-Kang Fang[3], Shushu Ruan[1,7], Jie Liu[1,7], Zhixian Wu[4,2], Xincheng Wang[2], Ahai Chen[2], Wei-Chao Jiang[6], Kiyoshi Ueda[2,5], Liang-You Peng[3,8*], Yuhai Jiang[2,4,1*]

[1]Shanghai Advanced Research Institute, Chinese Academy of Sciences, Shanghai & 201210, China.

[2]Center for Transformative Science and School of Physical Science and Technology, ShanghaiTech University, Shanghai & 201210, China.

[3]State Key Laboratory for Mesoscopic Physics and Frontiers Science Center for Nano-optoelectronics, School of Physics, Peking University, Beijing & 100871, China.

[4]School of Physics, Henan Normal University, Xinxiang & 453007, China.

[5]Department of Chemistry, Tohoku University, Sendai & 980-8578, Japan.

[6]Institute of Quantum Precision Measurement, College of Physics and Optoelectronic Engineering, Shenzhen University, Shenzhen & 518060, China.

[7]School of Future Technology, University of Chinese Academy of Sciences, Beijing & 100049, China.

[8]Collaborative Innovation Center of Extreme Optics, Shanxi University, Taiyuan & 030006, China.

*Corresponding author(s). Email(s):shenzhj2@shanghaitech.edu.cn; liangyou.peng@pku.edu.cn; jiangyh3@shanghaitech.edu.cn

†These authors contributed equally to this work.

Investigating the two-electron correlation of doubly excited states (DESs) in

the planetary atomic structure poses multiple conceptual and methodological challenges. Such highly correlated dynamics in a three-body Coulomb system can leave distinct signatures in the unique nonsequential above-threshold double ionization (NS-ATDI) exposed in a coherent laser field. Herein, we perform kinematically complete studies for multi-photon double ionization of cold strontium atoms. Our results reveal strongly favored NS-ATDI characterized by a series of band structures that demonstrate the energy and angular correlations of emitted two-electron pairs. These unprecedented characteristics reinforce the fact that both electrons are excited and ionized via the transition DESs, such that exotically strong two-electron correlations associated with atomic structure are relayed in the laser-driven time-dependent three-body system. The present findings transcend the traditional landscape in multi-photon double ionization and reshape our fundamental understanding of electron correlation in nature.

Electron correlation in Coulombic systems forms the cornerstone of many-body physics and governs the electronic energies and structures of complex microscopic and macroscopic systems. It is especially critical for strongly correlated materials including high-temperature superconductors (*1*) and colossal magneto resistance in transition-metal oxides (*2*). Studies on this topic often center on a prototypical platform provided by a helium or helium-like atom, where key phenomena including Fano resonance of doubly excited states (DESs) occur (*3–10*). These are the simplest three-body systems in nature, but complex enough to challenge the most advanced calculations (*11*). However, understanding the dynamics behind correlated electrons has been far from sufficient up to now.

DESs exhibit strong electron correlations characterized by interdependent motion of two electrons in position and momentum space (*12, 13*). When two electrons in high-lying DESs orbit the nucleus in distinct paths, analogous to planets orbiting a star, the system constitutes a so-called planetary atom (*14*) —a strongly correlated three-body system that has attracted increasing interest for decades (*11, 15–19*). Ion-yield and absorption spectroscopy have served as standard experimental tools to investigate planetary atoms (*19–21*), but such studies have been largely limited to measuring the energies of DESs. Direct access to the underlying structural dynamics has remained elusive, even though classical Kepler planetary motions in the eZe and Zee configurations have been predicted to exhibit angular stability (*11, 20, 22*). In these simplified one-dimensional pictures,

the eZe configuration corresponds to two electrons on opposite sides of the nucleus, whereas both electrons in the Zee configuration are on the same side. Remarkably, the angular correlation of the electrons is preserved from high-lying DESs into the continuum above the double ionization (DI) threshold, even across the quantum chaotic regime (*20, 22–24*).

DI serves as a sensitive probe of such correlated behavior, especially nonsequential DI, because the energy and momentum spectra of the two outgoing correlated electrons carry rich information that reveals the underlying physical mechanism. As an outstanding benchmark, single-photon DI studies have uncovered the canonical knock-out and shake-off ionization mechanisms. Investigations have been extended to two-photon (*25–29*), multi-photon (*30, 31*), and strong-field induced (*32–34*) DIs, revealing rich intrinsic ionization dynamics that remain active research frontiers. In the multi-photon strong perturbation regime, the above-threshold ionization phenomenon for two-electron emission—known as nonsequential above-threshold double ionization (NS-ATDI)—gives rise to highly correlated two-electron wave packets, in which both electrons absorb photons and share the excess energy in units of one photon. Using numerical solutions to the full-dimensional two-electron time-dependent Schrödinger equation (TDSE), Parker *et al.* (*35*) calculated ATDI for helium in high-coherence, high-brightness XUV laser fields and found a hint of nonsequential signals in the coexistence of primary sequential DI processes. There have been experimental reports on ATDI of rare gas atoms (*36, 37*) and molecules (*38*) induced by 400 nm lasers. To date, all experimental and theoretical studies indicate that sequential processes overwhelmingly dominate in ATDI.

Once high-lying DESs participate in NS-ATDI, a complex time-dependent three-body problem emerges, as the two-electron dynamics within the planetary structure evolves in the time-dependent laser field. The strong radial and angular correlations encoded in transient DESs (*39, 40*) can be accessed by detecting the emitted electron pairs, yielding distinct and revealing signatures in NS-ATDI. However, NS-ATDI studies involving DESs as intermediate transition states remain poorly developed because of substantial methodological challenges. Theoretically, single-photon perturbation theory and simple mean-field approaches are insufficient to describe this physical process. Furthermore, owing to multi-photon absorption, the coherence of the laser field is imprinted onto the highly correlated transition and emission processes, posing a great challenge for achieving a clear physical picture.

In this work, we use strontium atom—a helium-like system—as an ideal platform to investigate

two-electron correlations. In this system, a large number of DESs can be efficiently populated via multi-photon excitation with optical lasers (*19, 21, 41–43*), owing to much larger excitation cross sections than those of helium with one-photon absorption. Specifically, we perform the first kinematically complete study on ATDI by exploiting a state-of-the-art magneto-optical trap reaction microscope (MOTReMi) (*44–46*) and numerically solving the full-dimensional two-electron TDSE (*28, 34, 47*). A schematic diagram of Sr-MOTReMi is shown in Fig. 1. The cold strontium atoms created by laser cooling technologies were doubly ionized by femtosecond lasers. The momenta of Sr^{2+} ion and two photoelectrons in three dimensions were detected in coincidence with extremely high resolutions. The joint energy spectra (JES) from DI of the ground state $5s^2(^1S_0)$ show significantly dominant NS-ATDI features where two electrons present band structures and strong angular correlations as equally sharing excess energy. As intermediate transition states, DESs relay the electron correlations (see in the inset of Fig. 1), thereby enabling these distinct NS-ATDI features in the laser-driven time-dependent three-body system.

ATDIs at 800 nm

In Fig. 2, A to C, we present the JES for DI of $5s^2(^1S_0)$ driven by a linearly polarized 800 nm laser at various laser intensities, and electron-electron joint momentum spectra (JMS) can be seen in the Supplementary Fig. S1. These results clearly demonstrate the multi-photon absorption in a strong perturbative regime. The total energy for each ATDI structure is given by $E_{\text{sum}} = E_{e1} + E_{e2} = n\omega - I_{p1} - I_{p2} - 2U_p$, where ω is a photon energy, E_{e1} and E_{e2} represent the kinetic energies of the two photoelectrons , and I_{p1}= 5.7 eV/I_{p2} = 11.0 eV denote the first/second ionization potential. The number of absorbed photons n is estimated to be n = 12-15. $U_p \approx 0.4$ eV is the ponderomotive shift at a laser peak intensity $I = 6$ TW/cm^2. For the sequential DI of $5s^2(^1S_0)$, four and eight-photon are required for the ionization processes Sr $\rightarrow$ Sr^+ and $Sr^+ \rightarrow Sr^{2+}$, respectively. For the nonsequential DI of $5s^2(^1S_0)$, at least 11 photons are required. However, the 11-photon channel is effectively closed due to the shift induced by U_p.

Distinct NS-ATDI features are observed in the JES. Taking the 13-photon channel in Fig. 2B as an example, NS-ATDI shows a pronounced band pattern in the middle of the diagonal stripe, which is also characterized by circular arcs in the JMS (see Fig. S1 in the Supplementary). Two

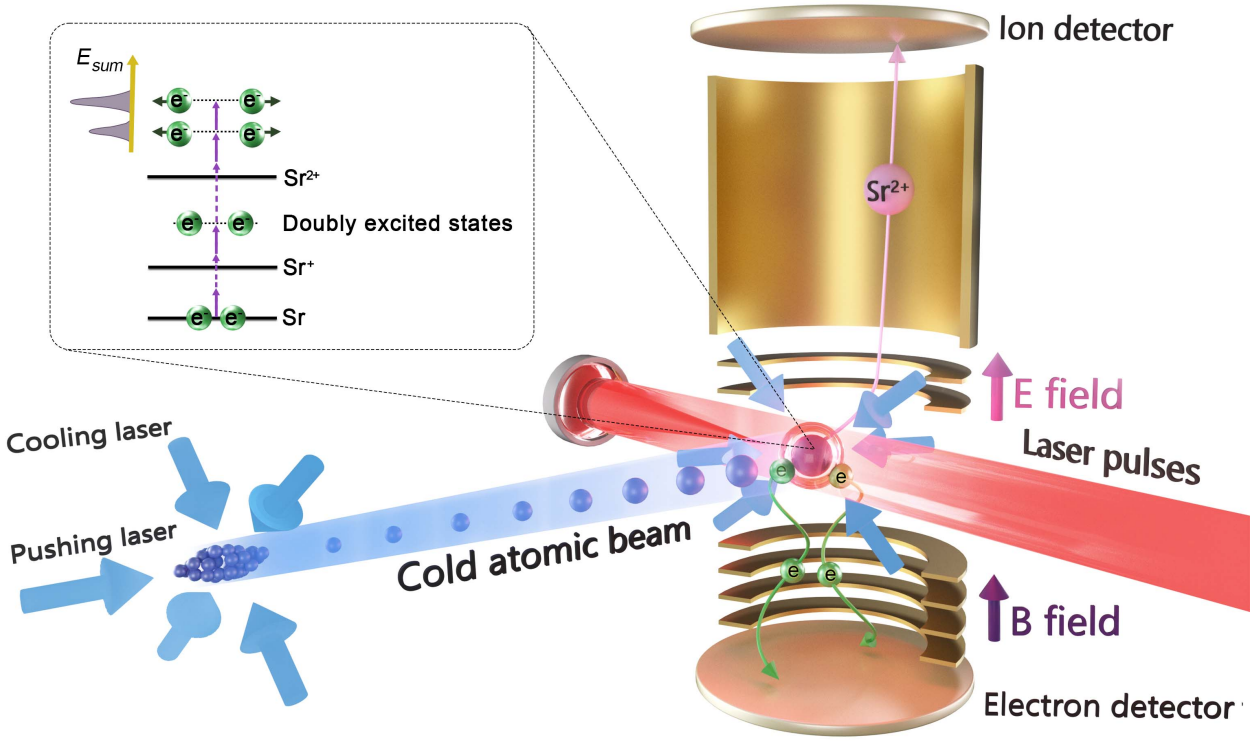

Fig.1. Schematic of the experimental setup. The continuum cold atomic beam is delivered to the reaction chamber by a red-shifted 461 nm pushing laser and further ionized by femtosecond lasers. The photoelectrons and recoil Sr^{2+} ion are guided to detectors at opposite ends by homogeneous magnetic and electric fields. The inset illustrates that a pair of electrons is ionized with correlated kinetic energies and emitted back-to-back by the proposed NS-ATDI mechanism via intermediate DESs.

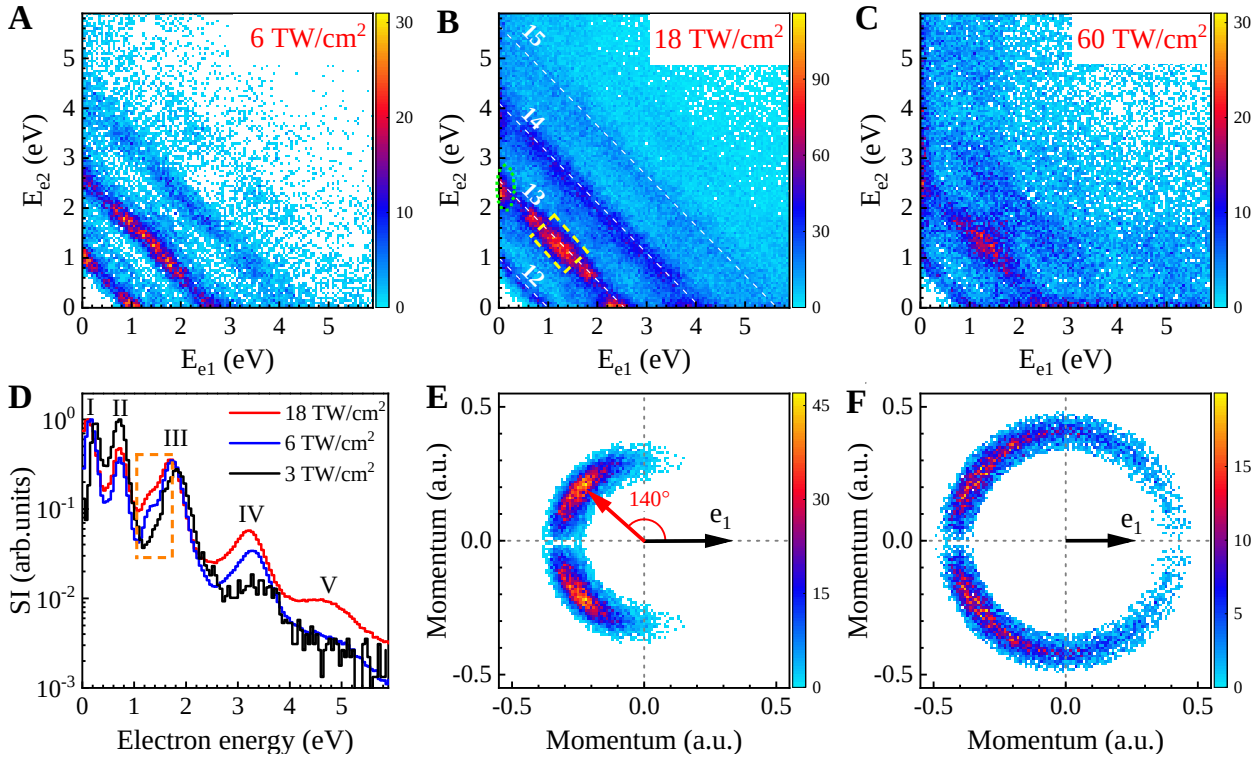

Fig.2. Electron energy spectra and correlated angular distributions (CADs). **(A** to **C)** Electron-electron JES at $I = 6$ TW/cm^2, 18 TW/cm^2, and 60 TW/cm^2. In (B), the white dashed line presents the zeroth to third ATDI where kinetic energy-sum of two electrons are constant and 12-15 indicate the number of photons absorbed. **(D)** Electron energy spectra for SI at $I = 3$ TW/cm^2, 6 TW/cm^2, and 18 TW/cm^2. The peaks I, III, IV and II correspond to electrons ionized from $5s^2\ ^1S_0$ with absorption of four-photon, the five-photon, six-photon and from $5s5p\ ^3P_2$ with three-photon absorption, respectively. The spectra are normalized to maxima of the peak I. **(E)** CADs of the second electron with $E_{e2} = 1.0-1.5$ eV as the first electron with $E_{e1} = 1.0-1.5$ eV emitted along the positive x-axis, corresponding to nonsequential ATDI electrons marked within the yellow dashed box in (B). **(F)** Same as (E) but for sequential ATDI with $E_{e2} = 2.2-2.6$ eV and $E_{e1} = 0-0.2$ eV, corresponding to electrons marked within the green dashed circle in (B).

emitted electrons share a total energy of $E_{\text{sum}} = 13\omega - I_{p1} - I_{p2} - 2U_p \approx 2.7$ eV, i.e., the kinetic energy of one electron increases as the other one decreases or vice versa, keeping their total energy constant. In contrast, sequential ATDI appears as island structures, one of which is indicated in the green dashed circle in Fig. 2B. In this case, the two sequentially ionized electrons have different kinetic energies, with $E_{e1} \approx 0.1$ eV from the single ionization (SI) of Sr (see also the peak I in Fig. 2D) and $E_{e2} \approx 2.4$ eV from the first order above-threshold ionization (ATI) of Sr^+. As the laser intensity increases, these features of NS-ATDI always prevail, although the stripes start to become broad because of the varying U_p over the entire laser pulse. The continuous distribution of these band structures constitutes a definitive hallmark of nonsequential ATDI and reflects two-electron energy correlations induced by multi-photon absorption. Most notably, the nonsequential signals are remarkably prominent, even comparable to those of sequential processes. These findings are quite different from previous theoretical and experimental ATDI studies (*35–37*), where sequential ATDIs always dominate absolutely. For sequential ATDI, two electrons are sequentially ionized from Sr and Sr^+ and their kinetic energies depend on the number of absorbed photons and the ionization potentials I_p, resulting in the absence of energy correlations.

Strong electron correlations are further manifested in the correlated angular distribution (CAD) of the two photoelectrons. For nonsequential electron pairs with nearly equal kinetic energies $E_{e1} = E_{e2} \approx 1.0 - 1.5$ eV located in the yellow dashed box in Fig. 2B, the CAD of one electron is plotted in Fig. 2E with the emission direction of the other fixed. The maximum ionization probability of the second electron appears at a relative emission angle $\theta_{12} = 140° \pm 10°$, indicated by a red arrow. The underlying mechanisms for the almost back-to-back emission might refer to the planetary atomic structure of the transition DESs, where the classical eZe configuration reflecting angular correlation survives significantly at relatively large angles between two electrons for the principal series (*20, 22*). For the principal series of DESs, the angle θ_{12} can approach 180° as closely as possible when approaching the DI threshold (*20, 22*). The enormous density of DESs might lead to nontrivial mixing, so even qualitative analysis of the DESs can be difficult. Nevertheless, a detailed and complete understanding still challenges current many-body theories and needs further investigation. The CAD for two sequential electrons is also shown in Fig. 2F. As expected, we observe almost isotropic distributions, i.e., one electron is emitted independently on the other, and no maximum in CAD is present. Note that progressively decreasing counts at relatively small angles

mainly results from the decreasing detection efficiency when two electrons arrive at the detector with approaching time. It has been confirmed that the CAD profile for NS-ATDI in Fig. 2E does not change after calibration with the data of sequential ATDI in Fig. 2F. In addition, the data in the regions very close to 0° and 180° are not physically meaningful due to the solid angles.

Considering the two-electron energy levels of strontium, at 800 nm, multi-photon resonant excitation to DESs should have been involved in the intermediate stage. Subsequently, the outermost two electrons in highly excited orbitals can be simultaneously ionized with nearly equal energy sharing and back-to-back emission. To verify the role of DESs, we plot the energy spectra of the SI in Fig. 2D at various laser intensities, where electrons are collected in coincidence with Sr^+ in order to avoid contributions from DI. Obviously, the distribution of the peak III, i.e., the first ATI, gradually varies from being symmetric to being asymmetric as the laser intensity increases, indicating the onset of autoionization decay from DESs. Most importantly, the autoionization features within the dashed box coincide closely with the emergence of NS-ATDI: At $I = 3$ TW/cm^2, we find no DI signals, while the autoionization of DESs is also negligible in Fig. 2D. As autoionization signals gradually present at $I = 6$ TW/cm^2 and 18 TW/cm^2, NS-ATDI structures accordingly become correspondingly prominent. However, it remains difficult to identify which specific DESs give rise to the spectral change near the first ATI because of the presence of a dense manifold of DESs. Nevertheless, for the first time, the above experimental observations present the scenario that dominating NS-ATDI features result from simultaneous emission of two electrons by coherent absorption of a couple of photons via one or a few DESs. The pronounced energy and angular correlations of two-electron pairs directly reflect the characteristic ionization dynamics of DESs.

Furthermore, we point out that the pathways to intermediate DESs can be manipulated by changing initial states and the ellipticity of the laser pulse, and subsequently modify the final JES results significantly. This assertion is supported by the ATDIs of the excited state of $5s5p(^1P_1)$, as shown in Fig. S2A of the Supplementary Materials. Interestingly, the JES presents visible and discrete island structures from sequential ATDIs, distinctly different from those in Fig. 2A. Changing the initial state from $5s^2(^1S_0)$ to $5s5p(^1P_1)$ will modify the character of intermediate transition states, which strongly perturbs electron correlations and ultimately suppresses the NS-ATDI channel. Meanwhile, by using a circularly polarized laser to ionize the $5s^2(^1S_0)$ atoms, sequential ATDIs with clear 'islands' structures cover the JES, as shown in Fig. S2B. This may be

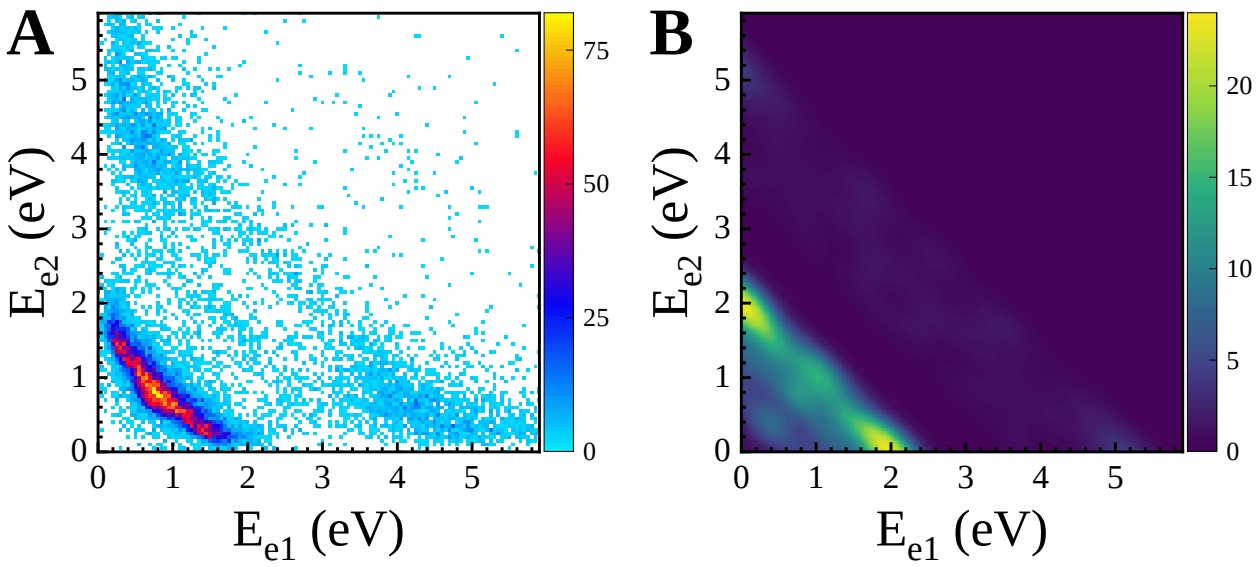

Fig.3. Same as Fig. 2, A to C but for linearly polarized 400 nm pulse at 18 TW/cm^2. (A) The experimental electron-electron JES; **(B)** Full-dimensional TDSE simulations.

explained as follows: once a circularly polarized photon is absorbed, the quantum number of the total angular momentum prefers to increase by one, so that it is highly detrimental to the formation of DESs during the absorption of more than 12 photons. Consequently, the strong correlation is intercepted during the transition stages, and the electrons tend to be released one-by-one.

ATDIs at 400 nm

To the best of our knowledge, so far, there is no report on a rigorous calculation of multi-photon induced ATDI at 800 nm or longer wavelengths for heavy atoms with two outermost electrons. The extremely large computation demand prohibits the attempt under current theoretical methodologies.

To further consolidate the above finding about the strong NS-ATDI, we carried out additional and independent measurements for a linearly polarized laser at 400 nm, whose results can be directly compared with our *ab initio* calculations.

In this shorter wavelength region, the field-induced electron collision is further suppressed and potential pathways of resonant excitation are also simplified. The experimental JES together with the results of the two-electron TDSE calculation are shown in Fig. 3, where the zero and first orders of ATDI are observed at I = 18 TW/cm^2. We note that the nonsequential DI band in the

experimental measurements remains the dominant structure located at $E_{e1} = E_{e2} \approx 0.8$ eV, whose overall features are reproduced by the theoretical calculation. The simultaneous excitation of DESs during the multi-photon absorption, as we discussed before, is very likely a universal correlation mechanism that induces the strong signal in the NS-ATDI channel.

Conclusions

With a state-of-the-art MOTReMi and the numerical solution to the full-dimensional two electron TDSE, we performed kinematically complete studies for multi-photon-induced ATDI in a helium-like heavy atom—strontium. Our experimental results exhibit prominently dominant NS-ATDI features. The emitted electron pairs exhibit strong energy and angular correlations, directly revealing ionization dynamics of the transient DESs. SI electron spectra reveal clear contributions from DES autoionization, consistent with NS-ATDI. This observation provides direct evidence that DESs are involved in mediating strong electron correlation. These remarkable, previously unobserved nonsequential features arise from pathways in which tightly bound two electrons, which simultaneously absorb coherent photons, are excited and ionized via intermediate DES ladders. Our work represents a significant advance in understanding strong two-electron correlation in laser-driven time-dependent three-body Coulomb systems and offers new insights into electron correlation dynamics across microscopic and macroscopic quantum phenomena.

Materials and methods

Experimental methods

A schematic diagram of the experimental setup, the Sr-MOTReMi (*44, 45*), is shown in Fig. 1. The hot strontium atoms evaporated in an oven are decelerated by a Zeeman slower laser beam and then precooled and trapped by two orthogonal pairs of retroreflected two-dimensional (2D) cooling laser beams. Subsequently, the 2D MOT is propelled to generate a cold atomic beam by a pushing laser beam and further cooled and trapped by a three-dimensional (3D) MOT configuration. Consequently, cold atomic targets for our setup can be prepared in the 2D MOT beam, molasses

beam, and 3D MOT. The 2D MOT beam delivers the continuous cold atomic beam employed for photoionization measurements of Sr($5s^2\ ^1S_0$). When the six 3D cooling laser beams are turned on in the reaction chamber without the gradient magnetic field, the molasses target containing cold atoms in the Sr($5s5p\ ^1P_1$) state is prepared for measurements. The 3D MOT is used for the overlapping determination of laser focus and atomic beams. We used a Ti:sapphire laser pulses with 800 nm and 400 nm wavelengths and 50 fs pulse duration (FWHM) at intensities of 3-60 TW/cm^2 to produce ions and electrons, which are collected in a 4π angle in a standard ReMi approach, see detailed configurations in Section 1 of Supplementary Materials. The momentum resolution for coincident Sr^+/Sr^{2+} and electrons along the longitudinal direction of the spectrometer is achieved up to 0.12 a.u. and 0.02 a.u., respectively, and slightly lower in the transverse plane.

Theoretical methods

The DI of the Sr atom is simulated using state-of-the-art numerical methods for solving the TDSE (*28, 34, 47*). Here, we assume that only two electrons are active and interact directly with the external laser field. The effects of inner-shell electrons and the nuclear core are incorporated through an angular-momentum-dependent pseudopotential, for details see Section 4 in Supplementary Materials. The two-electron wave function is expanded in coupled spherical harmonics, while its radial components are discretized using the finite-element discrete variable representation (FE-DVR) method. Both the maximum total angular momentum quantum number $L_{\max}$ and the maximum single-electron angular momentum quantum number $l_{\max}$ are set to 7. Nonuniform finite elements are employed, with finer element sizes near the core region and progressively larger elements at greater distances. Time propagation of the two-electron wave function is performed using the Lanczos method. During propagation, the two electrons are confined within a spherical box of radius 250 a.u.. The wave function is periodically split into inner and outer components. The inner part is always propagated numerically under the full Hamiltonian, whereas the outer part is propagated analytically using the Volkov propagator. At the end of the propagation, DI signals are extracted from both the inner and outer wave-function components.

References and Notes

1. P. W. Anderson, The Resonating Valence Bond State in La_2CuO_4 and Superconductivity. Science **235**, 1196–1198 (1987), doi:10.1126/science.235.4793.1196, https://www.science.org/doi/abs/10.1126/science.235.4793.1196.

2. M. Imada, A. Fujimori, Y. Tokura, Metal-insulator transitions. Rev. Mod. Phys. **70**, 1039 (1998), doi:10.1103/RevModPhys.70.1039, https://link.aps.org/doi/10.1103/RevModPhys.70.1039.

3. C. D. Lin, W.-C. Chu, Controlling Atomic Line Shapes. Science **340**, 694–695 (2013), doi:10.1126/science.1238396, https://www.science.org/doi/abs/10.1126/science.1238396.

4. C. Ott, et al., Lorentz Meets Fano in Spectral Line Shapes: A Universal Phase and Its Laser Control. Science **340**, 716–720 (2013), doi:10.1126/science.1234407, https://www.science.org/doi/abs/10.1126/science.1234407.

5. C. Ott, et al., Reconstruction and control of a time-dependent two-electron wave packet. Nature **516**, 374–378 (2014), doi:10.1038/nature14026, https://doi.org/10.1038/nature14026.

6. M. Kotur, et al., Spectral phase measurement of a Fano resonance using tunable attosecond pulses. Nature Communications **7**, 10566 (2016), doi:10.1038/ncomms10566, https://doi.org/10.1038/ncomms10566.

7. V. Gruson, et al., Attosecond dynamics through a Fano resonance: Monitoring the birth of a photoelectron. Science **354**, 734–738 (2016), doi:10.1126/science.aah5188, https://www.science.org/doi/abs/10.1126/science.aah5188.

8. A. Kaldun, et al., Observing the ultrafast buildup of a Fano resonance in the time domain. Science **354**, 738–741 (2016), doi:10.1126/science.aah6972, https://www.science.org/doi/abs/10.1126/science.aah6972.

9. C. Ott, et al., Strong-Field Extreme-Ultraviolet Dressing of Atomic Double Excitation. Phys. Rev. Lett. **123**, 163201 (2019), doi:10.1103/PhysRevLett.123.163201, https://link.aps.org/doi/10.1103/PhysRevLett.123.163201.

10. P. Zhang, et al., Resolving the phase of Fano resonance wave packets with photoelectron frequency-resolved optical gating. Nature Photonics **19**, 847–853 (2025), doi:10.1038/s41566-025-01715-z, https://doi.org/10.1038/s41566-025-01715-z.

11. G. Tanner, K. Richter, J.-M. Rost, The theory of two-electron atoms: between ground state and complete fragmentation. Rev. Mod. Phys. **72**, 497 (2000), doi:10.1103/RevModPhys.72.497, https://link.aps.org/doi/10.1103/RevModPhys.72.497.

12. U. Fano, Effects of Configuration Interaction on Intensities and Phase Shifts. Phys. Rev. **124**, 1866 (1961), doi:10.1103/PhysRev.124.1866, https://link.aps.org/doi/10.1103/PhysRev.124.1866.

13. R. P. Madden, K. Codling, New Autoionizing Atomic Energy Levels in He, Ne, and Ar. Phys. Rev. Lett. **10**, 516 (1963), doi:10.1103/PhysRevLett.10.516, https://link.aps.org/doi/10.1103/PhysRevLett.10.516.

14. I. C. Percival, Planetary atoms. Proceedings of the Royal Society of London. A. Mathematical and Physical Sciences **353**, 289–297 (1977), doi:10.1098/rspa.1977.0035, https://doi.org/10.1098/rspa.1977.0035.

15. K. Richter, D. Wintgen, Stable planetary atom configurations. Phys. Rev. Lett. **65**, 1965 (1990), doi:10.1103/PhysRevLett.65.1965, https://link.aps.org/doi/10.1103/PhysRevLett.65.1965.

16. U. Eichmann, V. Lange, W. Sandner, Positional correlation in laser-excited three-body Coulomb systems. Phys. Rev. Lett. **64**, 274 (1990), doi:10.1103/PhysRevLett.64.274, https://link.aps.org/doi/10.1103/PhysRevLett.64.274.

17. U. Eichmann, V. Lange, W. Sandner, Dipole structure of planetary atoms. Phys. Rev. Lett. **68**, 21 (1992), doi:10.1103/PhysRevLett.68.21, https://link.aps.org/doi/10.1103/PhysRevLett.68.21.

18. A. González-Melan, J. Madroñero, Nondispersive wave packets in planar helium. Phys. Rev. A **101**, 013414 (2020), doi:10.1103/PhysRevA.101.013414, https://link.aps.org/doi/10.1103/PhysRevA.101.013414.

19. M. Génévriez, C. Rosen, U. Eichmann, Structure and electron dynamics of planetary states of Sr below the Sr^+ $7d$ and $8p$ thresholds. Phys. Rev. A **104**, 012812 (2021), doi:10.1103/PhysRevA.104.012812, https://link.aps.org/doi/10.1103/PhysRevA.104.012812.

20. Y. H. Jiang, R. Püttner, D. Delande, M. Martins, G. Kaindl, Explicit analysis of chaotic behavior in radial and angular motion in doubly excited helium. Phys. Rev. A **78**, 021401 (2008), doi:10.1103/PhysRevA.78.021401, https://link.aps.org/doi/10.1103/PhysRevA.78.021401.

21. E. Marin-Bujedo, M. Génévriez, Autoionization of high-l core-excited Rydberg states of alkaline-earth-metal atoms. Phys. Rev. A **108**, 012816 (2023), doi:10.1103/PhysRevA.108.012816, https://link.aps.org/doi/10.1103/PhysRevA.108.012816.

22. J. Eiglsperger, J. Madroñero, Fluctuations in photoionization cross sections of singlet planar helium. Phys. Rev. A **82**, 033422 (2010), doi:10.1103/PhysRevA.82.033422, https://link.aps.org/doi/10.1103/PhysRevA.82.033422.

23. Y. H. Jiang, R. Püttner, D. Delande, M. Martins, G. Kaindl, Unreliability of the autocorrelation function as evidence for Ericson fluctuations. Phys. Rev. A **84**, 023402 (2011), doi:10.1103/PhysRevA.84.023402, https://link.aps.org/doi/10.1103/PhysRevA.84.023402.

24. Y. H. Jiang, Doubly excited helium: from strong correlation to chaos, Dissertation, Freie Universität Berlin, Berlin (2006), https://refubium.fu-berlin.de/handle/fub188/12235.

25. R. Moshammer, et al., Few-Photon Multiple Ionization of Ne and Ar by Strong Free-Electron-Laser Pulses. Phys. Rev. Lett. **98**, 203001 (2007), doi:10.1103/PhysRevLett.98.203001, https://link.aps.org/doi/10.1103/PhysRevLett.98.203001.

26. A. Rudenko, et al., Recoil-Ion Momentum Distributions for Two-Photon Double Ionization of He and Ne by 44 eV Free-Electron Laser Radiation. Phys. Rev. Lett. **101**,

073003 (2008), doi:10.1103/PhysRevLett.101.073003, https://link.aps.org/doi/10.1103/PhysRevLett.101.073003.

27. M. Kurka, et al., Two-photon double ionization of Ne by free-electron laser radiation: a kinematically complete experiment. Journal of Physics B: Atomic, Molecular and Optical Physics **42**, 141002 (2009), doi:10.1088/0953-4075/42/14/141002, https://doi.org/10.1088/0953-4075/42/14/141002.

28. W.-C. Jiang, J.-Y. Shan, Q. Gong, L.-Y. Peng, Virtual Sequential Picture for Non-sequential Two-Photon Double Ionization of Helium. Phys. Rev. Lett. **115**, 153002 (2015), doi:10.1103/PhysRevLett.115.153002, https://link.aps.org/doi/10.1103/PhysRevLett.115.153002.

29. M. Straub, et al., Differential Measurement of Electron Ejection after Two-Photon Two-Electron Excitation of Helium. Phys. Rev. Lett. **129**, 183204 (2022), doi:10.1103/PhysRevLett.129.183204, https://link.aps.org/doi/10.1103/PhysRevLett.129.183204.

30. H. Ni, S. Chen, C. Ruiz, A. Becker, Selection rules in the few-photon double ionization of the helium atom. J. Phys. B: At. Mol. Opt. Phys. **44**, 175601 (2011), doi:10.1088/0953-4075/44/17/175601, https://doi.org/10.1088/0953-4075/44/17/175601.

31. K. Henrichs, et al., Experimental evidence for selection rules in multiphoton double ionization of helium and neon. Phys. Rev. A **97**, 031405 (2018), doi:10.1103/PhysRevA.97.031405, https://link.aps.org/doi/10.1103/PhysRevA.97.031405.

32. B. Walker, et al., Precision Measurement of Strong Field Double Ionization of Helium. Phys. Rev. Lett. **73**, 1227–1230 (1994), doi:10.1103/PhysRevLett.73.1227, https://link.aps.org/doi/10.1103/PhysRevLett.73.1227.

33. T. Weber, et al., Correlated electron emission in multiphoton double ionization. Nature **405**, 658–661 (2000), doi:10.1038/35015033, https://doi.org/10.1038/35015033.

34. W.-C. Jiang, S.-G. Chen, L.-Y. Peng, J. Burgdörfer, Two-Electron Interference in Strong-Field Ionization of He by a Short Intense Extreme Ultraviolet Laser Pulse. Phys. Rev. Lett.

124, 043203 (2020), doi:10.1103/PhysRevLett.124.043203, https://link.aps.org/doi/10.1103/PhysRevLett.124.043203.

35. J. S. Parker, L. R. Moore, K. J. Meharg, D. Dundas, K. T. Taylor, Double-electron above threshold ionization of helium. J. Phys. B: At. Mol. Opt. Phys. **34**, L69–L78 (2001), doi:10.1088/0953-4075/34/3/103, https://doi.org/10.1088/0953-4075/34/3/103.

36. K. Henrichs, et al., Observation of Electron Energy Discretization in Strong Field Double Ionization. Phys. Rev. Lett. **111**, 113003 (2013), doi:10.1103/PhysRevLett.111.113003, https://link.aps.org/doi/10.1103/PhysRevLett.111.113003.

37. K. Henrichs, et al., Multiphoton double ionization of helium at 394 nm: A fully differential experiment. Phys. Rev. A **98**, 043405 (2018), doi:10.1103/PhysRevA.98.043405, https://link.aps.org/doi/10.1103/PhysRevA.98.043405.

38. X. Gong, et al., Channel-Resolved Above-Threshold Double Ionization of Acetylene. Phys. Rev. Lett. **114**, 163001 (2015), doi:10.1103/PhysRevLett.114.163001, https://link.aps.org/doi/10.1103/PhysRevLett.114.163001.

39. S. N. Pisharody, R. R. Jones, Probing Two-Electron Dynamics of an Atom. Science **303**, 813–815 (2004), doi:10.1126/science.1092220, https://www.science.org/doi/abs/10.1126/science.1092220.

40. X. Zhang, R. R. Jones, F. Robicheaux, Time-Dependent Electron Interactions in Double Rydberg Wave Packets. Phys. Rev. Lett. **110**, 023002 (2013), doi:10.1103/PhysRevLett.110.023002, https://link.aps.org/doi/10.1103/PhysRevLett.110.023002.

41. W. Huang, C. Rosen, U. Eichmann, W. Sandner, Multipole effects in the excitation of high-l doubly excited states in Sr. Phys. Rev. A **61**, 040502 (2000), doi:10.1103/PhysRevA.61.040502, https://link.aps.org/doi/10.1103/PhysRevA.61.040502.

42. G. Fields, X. Zhang, F. B. Dunning, S. Yoshida, J. Burgdörfer, Autoionization of very-high-n strontium Rydberg states. Phys. Rev. A **97**, 013429 (2018), doi:10.1103/PhysRevA.97.013429, https://link.aps.org/doi/10.1103/PhysRevA.97.013429.

43. M. Génévriez, M. Jungers, C. Rosen, U. Eichmann, Series of Molecularlike Doubly Excited States of a Quasi-Three-Body Coulomb System. Phys. Rev. Lett. **135**, 153002 (2025), doi: 10.1103/svsd-9mj3, https://link.aps.org/doi/10.1103/svsd-9mj3.

44. S. Ruan, et al., Magneto-optical trap reaction microscope for photoionization of cold strontium atoms. Phys. Rev. A **109**, 023118 (2024), doi:10.1103/PhysRevA.109.023118, https://link.aps.org/doi/10.1103/PhysRevA.109.023118.

45. S. Ruan, et al., Multichannel photoionization of cold strontium atoms. Phys. Rev. A **110**, 033114 (2024), doi:10.1103/PhysRevA.110.033114, https://link.aps.org/doi/10.1103/PhysRevA.110.033114.

46. H. Ma, et al., Complete Characterizations of Intermediate and Final State Wave Functions with Photoionization of Polarized Rb. Phys. Rev. Lett. **134**, 123204 (2025), doi:10.1103/PhysRevLett.134.123204, https://link.aps.org/doi/10.1103/PhysRevLett.134.123204.

47. L.-Y. Peng, W.-C. Jiang, J.-W. Geng, W.-H. Xiong, Q. Gong, Tracing and controlling electronic dynamics in atoms and molecules by attosecond pulses. Physics Reports **575**, 1–71 (2015), doi:https://doi.org/10.1016/j.physrep.2015.02.002, https://www.sciencedirect.com/science/article/pii/S0370157315001489.

Acknowledgments

Funding: This work is supported by the National Key Research and Development Program of China (Nos. 2022YFA1604302 and 2024YFA1612101), the National Natural Science Foundation of China (Nos. 12334011, 12234002, 12541505, 12204498, 12174284 and 12474346), and the Natural Science Foundation of Henan (Grant No. 252300421304). We also acknowledge support from the Shanghai-XFEL beamline project (SBP) (Grant No. 31011505505885920161A2101001) and the computational resource of the HPC platform in ShanghaiTech University.

Author contributions: Y.J. supervised the project. X.Y., Z.S., S.R., J.L., Z.W., X.W., and Y.J. performed the experiments. Y.H., Y.F., W.J., and L.Y.P. performed the simulations. X.Y., Z.S., and

Y.J. analyzed the data. Y.J., Z.S., and X.Y. wrote the manuscript after in-depth discussions with K.U., A.C., and with important input from all other authors.

Competing interests: The authors have no competing interests to declare

Data and materials availability: The data and materials that support the plots within this article are available from the corresponding authors upon reasonable request.

Supplementary Materials for

Strong Electron Correlation Identified in Planetary Atomic Structure

Xinglong Yu *et al.*

**Corresponding author(s). Email(s):Zhenjie Shen, shenzhj2@shanghaitech.edu.cn; Liang-You Peng, liangyou.peng@pku.edu.cn; Yuhai Jiang,jiangyh3@shanghaitech.edu.cn*

This PDF file includes:

Materials and Methods

Figs. S1 and S2

Table S1

References

Materials and Methods

Details of the experiment

The Sr-MOTReMi setup employed in the experiments comprises two main components: a two-dimensional magneto-optical trap (2D MOT) that provides the cold atomic beam, and a reaction microscope for detecting the momentum vectors of recoil ions and electrons. More details have been reported in our previous work (*1*).

Solid strontium is heated in an oven to ~ 460 °C to produce a thermal atomic beam into the 2D MOT chamber. The hot strontium atoms are decelerated by a Zeeman slower laser beam and subsequently precooled and captured by two pairs of orthogonally arranged and retroreflected 2D cooling laser beams to form the 2D MOT. A pushing beam with an intensity of 65 mW/cm^2 serves to transfer the 2D MOT to the reaction region, generating the cold atomic beam with the flux of $\sim 2 \times 10^7$ atoms/s. A weak uniform electric field of 1.7 V/cm accelerates the recoil ions and electrons, with a collinear homogeneous magnetic field ($\sim$ 4 G) applied to confine the electron trajectories. The acceleration lengths for recoil ions and electrons are 112.5 mm and 222.5 mm, respectively. The accelerated ions travel through a 430 mm drift region, whereas electrons undergo no drift section. These charged particles are collected by ion and electron detectors, each with a diameter of 80 mm, covering a 4π solid angle. By measuring the time of flight (TOF) and the impact positions on the detectors, the three-dimensional momentum vectors of the recoil ions and electrons can be reconstructed. The momentum resolution for coincident Sr^+/Sr^{2+} and electrons along the longitudinal direction of the spectrometer reaches to 0.12 a.u. and 0.02 a.u., respectively, and is slightly worse in the transverse plane. To suppress potential false coincidence effects, the momentum conservation cutoff of $|p_{z,Sr^+} + p_{z,e}| < 0.5$ a.u. is imposed for single ionization (SI), and $|p_{z,Sr^{2+}} + p_{z,e1} + p_{z,e2}| < 0.5$ a.u. for double ionization (DI). Additionally, in the context of DI measurements, the probability of ionizing two atoms with the same laser pulse is below 2%.

We employed a Ti:sapphire laser system that delivers linearly polarized pulses centered at 800 nm with a pulse duration of 50 fs and a repetition rate of 1 kHz. The laser intensity can be continuously adjusted using a half-wave plate in conjunction with a linear polarizer. The pulse intensity is calibrated using the ponderomotive shift U_p of electrons from SI of ground state atoms. At intensities below 6 TW/cm^2, the ground state atoms are directly ionized via the absorption of

four photons, and the ac Stark shift is negligible. Hence, the measured electron energy shift is ascribed solely to U_p, from which the intensity is derived via $I = U_p \times 4\omega^2$ (in atomic units). The laser intensities at higher power levels are determined by scaling this low intensity value according to the power ratio measured with a calibrated meter. Based on this procedure, the peak intensity of the 800 nm pulses used in our experiments is estimated to be 3-60 TW/cm^2. The linearly polarized 400 nm pulse is generated by doubling the frequency of 800 nm through a β-barium borate crystal, and the peak intensity is determined to be 18 TW/cm^2. Across the intensity range studied, the maximum electron counting rate remained below 0.1 electrons per laser pulse, with a consistent ion-to-electron ratio of approximately 1:3.

The cold atomic beam contains strontium atoms in both the ground state and the metastable state $5s5p\ ^3P_2$. The $5s5p\ ^3P_2$ state is a dark state that is generated and accumulates within the 2D MOT and is subsequently transported together with ground state atoms into the reaction chamber and exhibits a spatial distribution peaked away from the laser focus. The SI of $5s5p\ ^3P_2$ is easily achieved, whereas above-threshold ionization (ATI) and above-threshold double ionization (ATDI) involving the absorption of more photons are strongly suppressed. The molasses target is created by 3D cooling laser beams without gradient magnetic field, with $\sim 10\%$ of the atoms populated into the $5s5p\ ^1P_1$ state. In comparison, the $5s5p\ ^3P_2$ state generated in the reaction region by the 3D cooling beams accounts for only approximately 1/150000 of the population in the $5s5p\ ^1P_1$ state, rendering it negligible. Consequently, DI originating from the $5s5p\ ^3P_2$ state is not discussed in this work.

Electron-electron joint momentum spectra

Fig. S1 presents the electron-electron joint momentum spectra (JMS) of strontium atoms in the ground state irradiated at intensities of 6 TW/cm^2, 18 TW/cm^2, and 60 TW/cm^2. A series of circular arcs arise from the incoherent superposition of sequential and nonsequential ATDI. The strong correlation of electrons leading to nonsequential ATDI ($P_{e1} \approx P_{e2}$) dominates the DI process, consistent with the electron-electron joint energy spectra (JES) presented in Fig. 2, A to C of the main text. For the linearly polarized pulse at an intensity of 6 TW/cm^2 ($U_p \approx 0.4$ eV), the Keldysh parameter is calculated to be 2.7, indicating an ionization regime dominated by multi-photon

absorption. The maximum energy of the recolliding electron is approximately $3.2 \times U_p \approx 1.3$ eV, this energy is substantially below the second ionization potential of Sr (11.0 eV) and even lower than the energy of the first excited state of Sr^+ ($4p^6 4d$, 1.8 eV). Therefore, direct ionization (e, 2e) and recollision excitation followed by ionization can be excluded. Instead, electrons are populated in intermediate transition doubly excited states (DESs) by absorbing multiple photons, which leads to the stabilization of ATDI energy at elevated intensities.

ATDIs with different initial state and ellipticity

We experimentally study the ATDIs of the excited state of Sr($5s5p\ ^1P_1$) using the molasses target, as presented in Fig. S2A. Interestingly, the JES in Fig. S2A present visible and discrete island structures, indicating sequential ATDIs and distinctly different from Fig. 2A in the main text. Here, the DI of $^1P_1$ requires two fewer photons than $^1S_0$, leading to the dominance of sequential ATDI with island structures.

One notices that even this kind of slight distinguishability of electrons in the initial state is critical to disrupt the strong correlation of electrons and to significantly suppress the nonsequential characteristic in the ATDI. This partly supports the present scenario that both electrons are ionized simultaneously via transition DESs, where they jump together via DESs ladders forming planetary atomic structure.

Meanwhile, we employ a circularly polarized laser to study ATDIs. Sequential ATDIs with clear 'islands' structures over the JES shown in Fig. S2B and the characteristic of nonsequential ATDIs completely disappears. Once a circularly polarized photon is absorbed, the quantum number of total angular momentum prefers to increase by one, so that it is highly detrimental to maintaining the overlap among the two-electron wave packets during the absorption of more than 12 photons. It is much more difficult for the pair of electrons to continuously absorb photons until they emit simultaneously. Instead, the correlation is broken, and the electrons intend to be released one-by-one. This is a possible reason why sequential channels dominate under this condition.

Details of the theoretical method

In the numerical simulation, the two-electron wave function is evolved under the following Hamiltonian

$$H = -\frac{1}{2}\nabla_1^2 - \frac{1}{2}\nabla_2^2 + V(\boldsymbol{r}_1) + V(\boldsymbol{r}_2) - \mathrm{i}\boldsymbol{A}(t)\cdot(\boldsymbol{\nabla}_1 + \boldsymbol{\nabla}_2) + \frac{1}{|\boldsymbol{r}_1 - \boldsymbol{r}_2|}, \tag{S1}$$

where the laser field is

$$\boldsymbol{A}(t) = A_0\hat{z}\sin^2\frac{\pi t}{T}\cos\omega t, \tag{S2}$$

in which $T = 40\,\mathrm{fs}$ is the total length of the pulse, and A_0 is chosen to match a peak intensity of $I = 18\,\mathrm{TW/cm^2}$. The pseudopotential is (*2*)

$$V(\boldsymbol{r}) = -\frac{Q}{r} + \sum_l \left\{ B_l \exp(-\beta_l r^2) - \frac{\alpha_d}{2r^4}\left[1 - \exp\left(-\frac{r^6}{r_{c,l}^6}\right)\right]\right\} P_l, \tag{S3}$$

in which P_l is a projection operator onto the subspace of angular quantum number l, $Q = 2$ is the effective charge, and $\alpha_d = 5.813$ is the polarizability of the strontium core (*3*). The remaining l-dependent parameters are listed in Table S1.

The basis set chosen for this calculation consists of the coupled spherical harmonics $Y_{l_1 l_2}^{LM} = \sum_m \langle l_1\, l_2\, m\, (M-m)|L\, M\rangle$ for the angular part and a Gauss-Lobatto FE-DVR with non-uniform element sizes for the radial part. The angular momentum cutoff is chosen to be $L_{\max} = l_{\max} = 7$ and the grid boundary is $r_{\max} = 250\,\mathrm{a.u.}$.

The initial state $5s^2$ is obtained with the Lanczos method, then time-propagated via the Krylov method. Through the course of propagation, a mask function is periodically applied to prevent reflection. At each application, the split-off part consisting of amplitudes near the grid boundary is projected into momentum space and evolved subsequently according to a simple Volkov phase: $\exp\{-\mathrm{i}[k_1^2/2 + k_2^2/2 + \boldsymbol{A}\cdot(\boldsymbol{k_1} + \boldsymbol{k_2})]t\}$.

The final wave function is projected into the momentum space and then combined with the coherent sum of all previous split-off parts to obtain the momentum distribution $P(\boldsymbol{k}_1, \boldsymbol{k}_2)$, which can be further integrated over angles for the JES.

Absorption of outgoing waves

Through the course of propagation, a mask function in the form of $f(r_1) \cdot f(r_2)$ is applied periodically, with $f(r)$ given by:

$$f(r) = \begin{cases} 1, & r < r_c, \\ 1 - \left(\dfrac{r - r_c}{r_d}\right)^2 \cdot \left(3 - 2 \cdot \dfrac{r - r_c}{r_d}\right), & r_c \leq r \leq r_c + r_d, \\ 0, & r > r_c + r_d, \end{cases} \tag{S4}$$

with parameters $r_c = 100\,\text{a.u.}$ and $r_d = 100$ a.u. This mask function is chosen to preserve the continuity of the derivative at both r_c and $r_c + r_d$ to provides a smooth splitting.

Momentum space projection

The basis of the momentum space are approximate two-electron scattering states, taken to be the symmetrized product of two independent single particle scattering states:

$$\phi_{\boldsymbol{k}_1\boldsymbol{k}_2}(\boldsymbol{r}_1, \boldsymbol{r}_2) = \frac{1}{\sqrt{2}} \left[\phi_{\boldsymbol{k}_1}(\boldsymbol{r}_1)\phi_{\boldsymbol{k}_2}(\boldsymbol{r}_2) + \phi_{\boldsymbol{k}_1}(\boldsymbol{r}_2)\phi_{\boldsymbol{k}_2}(\boldsymbol{r}_1)\right]. \tag{S5}$$

The single-particle scattering states are the ingoing solutions of the single-electron Schrödinger equation, with the form

$$\phi_{\boldsymbol{k}}(\boldsymbol{r}) = \sum_{l=0} (2l + 1)\mathrm{i}^l \mathrm{e}^{-\mathrm{i}\delta_l} R_{kl}(r) P_l(\cos\theta), \tag{S6}$$

where δ_l is the Coulomb phase shift to be determined.

The l-separated radial solutions R_{kl} are obtained by solving the radial equation

$$\left[-\frac{1}{2}\frac{\mathrm{d}^2}{\mathrm{d}r^2} - \frac{1}{r}\frac{\mathrm{d}}{\mathrm{d}r} + \frac{l(l+1)}{2r^2} + V_l(r) - \frac{1}{2}k^2\right] R_{kl}(r) = 0, \tag{S7}$$

with the Killingbeck-Miller method (*4*) with sufficiently small radial step h. To determine the phase shift δ_l and normalization constant a, the unnormalized $\tilde{R}_{kl}(r)$ is compared against the free space solution with phase shift in the asymptotic region:

$$R_{kl}(r) = a \cdot \tilde{R}_{kl}(r) \xrightarrow[r\to\infty]{} \frac{\sin(kr - l\pi/2 + \delta_l)}{kr}. \tag{S8}$$

In practice, this is done by comparing the position and magnitude of any single extremum of $kr\tilde{R}_{kl}(r)$ against the sine function at $kr \approx 1000$.

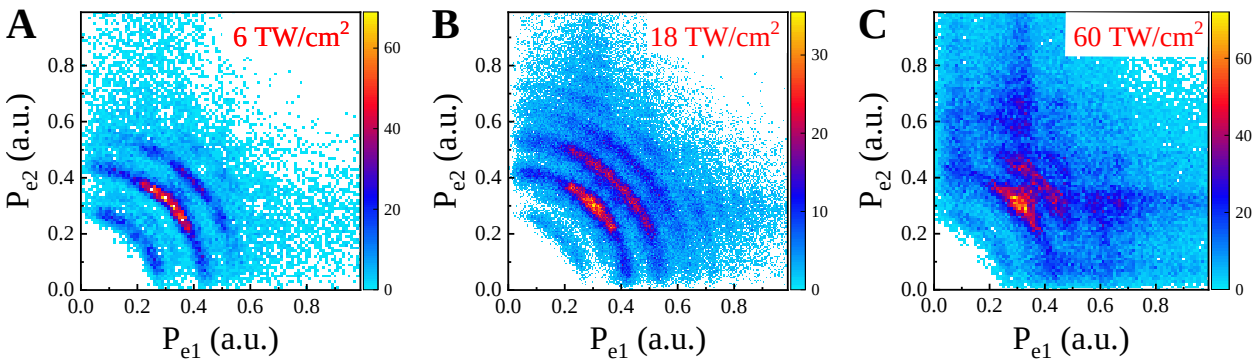

Fig.S1. Electron–electron JMS of Sr ($5s^2\ ^1S_0$) measured under linearly polarized 800 nm pulse at intensities of **(A)** 6 TW/cm^2 , **(B)** 18 TW/cm^2 and **(C)** 60 TW/cm^2.

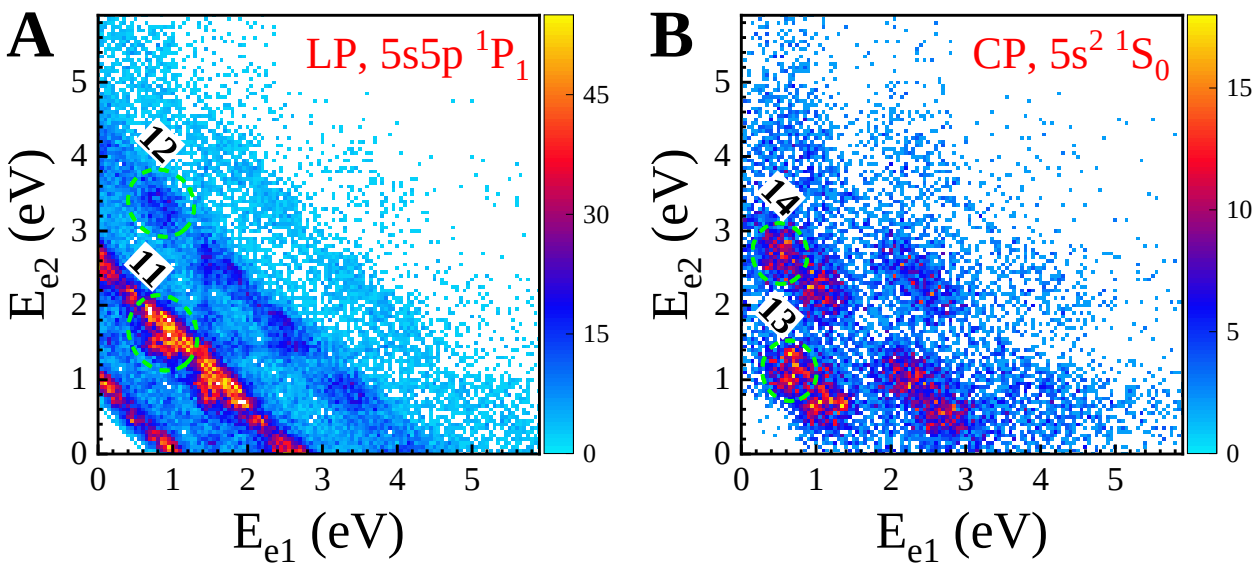

Fig.S2. The initial-state- and ellipticity-dependent JES. (A) The JES from a mixture target of the ground state and the singly excited state $5s5p\ ^1P_1$ by a linearly polarized (LP) pulse at I=6 TW/cm^2. **(B)** The JES from the ground state but in a circularly polarized (CP) pulse at I=18 TW/cm^2. The corresponding numbers of photons required for ATDI are indicated in each channel.

l	0	1	2	≥ 3
B_l	15.387	5.077	−2.248	0
β_l	0.7962	0.4212	0.4927	0
$r_{c,l}$	2.022	1.950	2.204	1.761

Table.S1. Parameters of the pseudopotential.

References and Notes

1. S. Ruan, et al., Magneto-optical trap reaction microscope for photoionization of cold strontium atoms. Phys. Rev. A **109**, 023118 (2024), doi:10.1103/PhysRevA.109.023118, https://link.aps.org/doi/10.1103/PhysRevA.109.023118.

2. P. Fuentealba, L. von Szentpaly, H. Preuss, H. Stoll, Pseudopotential calculations for alkaline-earth atoms. Journal of Physics B: Atomic and Molecular Physics **18**, 1287 (1985), doi:10.1088/0022-3700/18/7/010, https://dx.doi.org/10.1088/0022-3700/18/7/010.

3. K. Guo, G. Wang, A. Ye, Dipole polarizabilities and magic wavelengths for a Sr and Yb atomic optical lattice clock. Journal of Physics B: Atomic, Molecular and Optical Physics **43**, 135004 (2010), doi:10.1088/0953-4075/43/13/135004, https://dx.doi.org/10.1088/0953-4075/43/13/135004.

4. J. P. Killingbeck, Microcomputer calculations in physics. Reports on Progress in Physics **48**, 53 (1985), doi:10.1088/0034-4885/48/1/002, https://doi.org/10.1088/0034-4885/48/1/002.